ERWIN L. HAHN INSTITUTE FOR MAGNETIC RESONANCE IMAGING

ANNUAL REPORT 2019

Erwin L. Hahn Institute for Magnetic Resonance Imaging
Kokereiallee 7
45141 Essen
Germany

fon +49 (0) 201 1836070
fax +49 (0) 201 1836073
hahn-institute.de

Published by the Erwin L. Hahn Institute for Magnetic Resonance Imaging.

Preface

2019 has been a special year in many regards for the Erwin L. Hahn Institute and its members. Most notably, in September the Deutsche Forschungsgesellschaft (DFG) approved our grant for the upgrade of our MRI system, which is scheduled for 2020. The ELH is delighted by the decision of the DFG and is looking forward to working with the new system.

We are also delighted that in 2019 the Ruhr-University Bochum joined the ELH with a PI group led by Prof. Dr. Dr. h.c. Onur Güntürkün, which we are sure will create exciting new synergies and interdisciplinary exchange.

For the 2019 Erwin L. Hahn Lecture, the ELH returned to the relaxed atmosphere of the OKTOGON. Prof. Dr. Heidi Johansen-Berg from the University of Oxford held a fascinating lecture on "Studying Connectivity and Plasticity in the Human Brain with MRI". Her lecture was preceded by a series of very well received workshops on various MRI-related topics.

Prof. Johansen-Berg also marked the first female keynote speaker invited to the Erwin L. Hahn Lecture and urged for more representation of women in the sciences, something which the ELH strongly agrees with and will strive for in upcoming workshops and events. At the same event Dr. Stefan Rietsch was awarded the ELH Young Investigators Award for his dissertation thesis: "Development and Evaluation of Radio Frequency Antennas for 7 Tesla Ultrahigh-Field Magnetic Resonance Imaging". The 2020 lecture will take place on October 28th, once again at the OKTOGON, so mark your calendars and clear your agendas!

On October 3rd, the ELH took part in a nation-wide Open House event "Maus Türöffner-Tag", initiated by the long-running German children' s TV program "Die Sendung mit der Maus". The day brought many visitors of all ages to the ELH, which received overwhelmingly positive feedback from its visitors both young and old.

Once again the ELH's annual report covers a broad range of subjects, as diverse as the current eight PI groups situated at the ELH and their research fields. One exciting example of ELH activities regarding technical solutions for ultra-high field MRI is the optimization of the 32-channel transmit system. Another highlight is the improvement of high-resolution raw data acquisition and analysis methods for laminar fMRI. We have also successfully continued our scientific work on both brain and body. The studies on the involvement of the cerebellum in emotional learning and on the brain correlates of human-robot interaction are examples of our fMRI studies in 2019. We also contributed to clinical applications of 7T MRI, for example by developing techniques, which help to optimize lymph node staging in patients with rectal cancer. Additionally, we investigated very specific research questions in unique samples. In this context, we have scanned a group of American Football Players at the ELH institute. Several other exciting projects and ELH activities are described in this annual report. We are thankful for the major contributions of our partners and looking forward to a productive continuation in 2020.

Matthias Brand

Essen, Spring 2020.

Goodbye, Scanner!

When the Erwin L. Hahn Institute for MRI opened its doors in 2006 and the 7 Tesla ultra-high-field MRI scanner moved in, it was only the 2nd 7 Tesla MRI system in Germany, and the 6th 7 Tesla MRI worldwide. To say that it has been the heart of the ELH would be an understatement, and while over the past fourteen years the ELH has seen many of its staff members come and go, the 7 Tesla has been one of the main constants.

To see it go has been a bittersweet experience, as it is the very same appliance that Erwin L. Hahn, who discovered the spin echo and was kind enough to allow the ELH to take its name after him, visited in 2009. The ELH's MRI scanner saw the first body coil for 7 Tesla, engineered by ELH scientists, and was used only last summer by the Medical Faculty of the University Duisburg-Essen to demonstrate indications of previously unknown blood vessels in human bones.

But as always, still stand and scientific research are polar opposites, and so we must say goodbye to our trusty 7 Tesla MRI this June (2020).

In 2019, the ELH was granted the means to acquire a new state of the art 7 Tesla MRI system by the Deutsche Forschungsgemeinschaft (DFG). And as we write this, preparations for the reconstruction and magnet exchange are in progress at the ELH. For the first time in fourteen years, there is currently no noteworthy magnetic field anywhere in the Erwin L. Hahn Institute.

The exchange, of course, is made more difficult by the ongoing Corona pandemic, but safety protocols are in place to ensure everyone's health. We are expecting to have the new scanner operational in autumn 2020 and scientists and staff alike are excited for the new arrival and the future research the new 7 Tesla MRI system will enable and nurture at the ELH. Stay tuned till the (new) strongest magnet in the Ruhr Valley area is steadily ramped up to ultrahigh field.

Zero Tesla - For the first time in fourteen years there is no noteworthy magnetic field anywhere in the Erwin L. Hahn Institute– as evident by the metal ladder casually placed beside the MRI scanner. On any other day in the past fourteen years, this would have been impossible.

2006 – the 7 Tesla MRI scanner moves into the Erwin L. Hahn Institute for MRI.. At the time, it was only the second 7 Tesla MRI scanner in Germany.

View from the operation room into the scanner room.

The heart of the Erwin L. Hahn Institute: The 7 Tesla MRI scanner that has served countless doctors, scientists, PhD, MA & BA students as well as interns over the past fourteen years.

A 32-channel transmit system add-on for 7 Tesla body imaging

At ultra-high field, severe excitation inhomogeneities affect the quality of imaging when using volume coils for transmission, which are standard at lower field strengths. In an effort to cope with these problems, multi-channel methods have been developed that statically (RF shimming), semi-dynamically (spokes, k-t-points, TIAMO[1]), or dynamically (Transmit Sense) modulate the amplitude and phase of input signals for multi-channel transmit arrays. To make use of these methods, suitable hardware is a prerequisite. Here we present a 32-channel transmit system as an add-on to a commercial 7 Tesla MRI (Magnetom 7T, Siemens Healthineers, Erlangen, Germany).

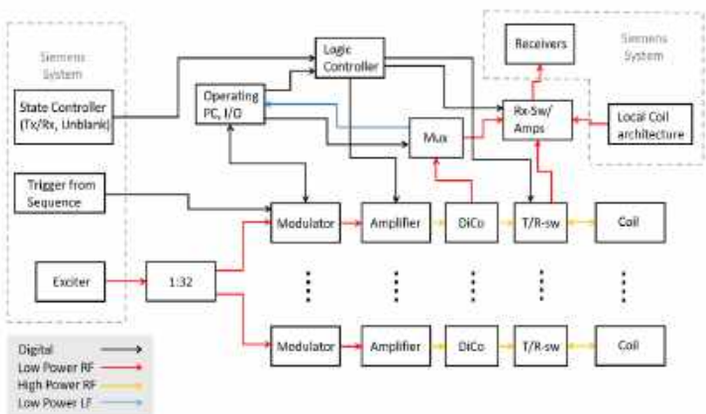

Figure 1: Simplified schematic overview of the add-on system

The add-on system requires only one analog and three digital input signals from the vendor-provided MRI system. A simplified overview is given in Figure 1. The add-on system receives the unblank signal and the T/R signal from the state controller to switch into the correct state, the single-channel RF pulse from the system's exciter, and a digital trigger from the sequence to set the modulators. Furthermore, the add-on system feeds back received signals from either the transmit coil or dedicated receive coils as well as transmit pulse supervision signals to the original system receivers. Apart from these interfaces, the systems are independent from one another.

The signal from the MRI system's master exciter can be switched to the 32-channel system and is then split into 32 channels with equal amplitudes and phases. Each of the 32 signals is then fed to an I/Q modulator[2] (Figure 2A and B). The modulators are programmed by an operating PC and assume a new state on each trigger signal from a running pulse sequence with a sampling rate of up to 100 kHz. The modulated signals are fed into 1 kW LDMOS amplifiers[3] situated directly at the magnet (Figure 2C and D). The high-power RF signals are fed through directional couplers. The forward and reflected power are measured with logarithmic amplifiers and sent to a supervision computer. In addition, the forward signal can be fed directly into the receive chain via a switch (Figure 2E) for complex pulse supervision. An integrated body coil[4] with additional electronics (Figure 2F-H) is connected to the high-power output of the directional couplers via T/R switches, so that the body array can be used both as a transmit and receive array. A logic controller dynamically sets the states of the different components with logic implemented in hardware for increased robustness. The system can be run with reception either from the body coil or a local array.[5] Via the controller's software, the add-on system can be switched to an offline state in which it is transparent to the original system. In this configuration, the power amplifiers and receive amplifiers are switched off, all switches are

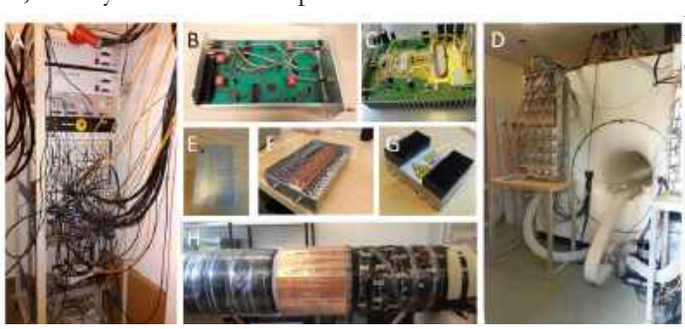

Figure 2: A) 19" rack in equipment room containing power supplies, control and supervision computers, modulators, and control electronics; B) Modulator cassette for 2 channels; C) LDMOS power amplifier; D) 16 amplifiers in rack directly at the back side of magnet; E) 32-ch receive chain switch; F) 2nd-stage receive amplifiers; G) magnet room PIN diode power supply for body coil; H) integrated 32-ch body coil.

Stephan Orzada, Klaus Solbach, Marcel Gratz, Sascha Brunheim, Thomas M. Fiedler, Sören Johst, Andreas K. Bitz, Samaneh Shooshtary, Ashraf Abuelhaija, Maximilian Voelker, Stefan H. G. Rietsch, Oliver Kraff, Stefan Maderwald, Martina Flöser, Mark Oehmigen, Harald H. Quick, Mark E. Ladd

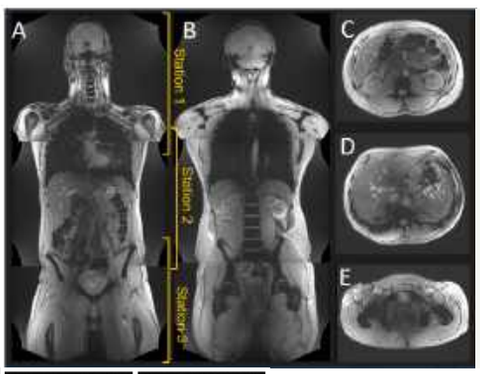

Figure 3: Gradient echo images acquired with the integrated 32-ch body coil in a male volunteer (92kg, 182cm). A-B) Coronal images acquired with a 50 cm field of view and 10 cm overlap between the stations. C-E) Axial slices acquired at different z-positions. All images were acquired using TIAMO for image homogenization.

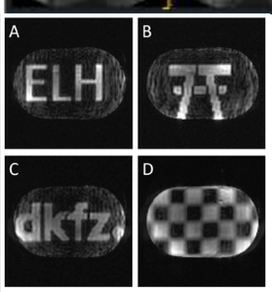

Figure 4: pTx images acquired in a homogeneous body phantom (340 mm width, 207 mm height, 500 mm length) filled with tissue-simulating liquid. A-C) institution logos, D) checkerboard pattern.

switched to a state where the standard signal paths are adopted, and the body coil is switched to a detuned state.

Figure 3 shows a set of images demonstrating first results for large field of view in-vivo body imaging acquired with the 32-channel system in a male volunteer (92 kg, 1.85 m). The head to thigh images (Figure 3A and B) were acquired in only 3 stations using TIAMO. Each station has a length of 50 cm in the z-direction, and the table was moved by 40 cm between acquisitions. Images Figure 3C-E show axial slices in different positions. No complete signal dropouts are visible, although only pre-set modes (Cp+ and Cp2+) were used for the TIAMO algorithm. Figure 4 shows 2D spatially selective pTx excitation results from a homogeneous body phantom (340 mm width, 207 mm height, 500 mm length). The integrated body array was used for transmission and reception. Figure 5 shows the first in vivo full pTx results. Figure 5A-G show slices from 3D gradient echo data sets. Figure 5A-C were acquired with TIAMO in breath hold as an anatomical reference. Figure 5D shows the same sequence acquired during free breathing. Figure 5E-G show images from a 3D dataset acquired with 2D spatially selective excitation targeted at the spine during free breathing. Only few motion artifacts are visible. Figure 5H shows the target for the optimization. QA tests verified that the MRI system works normally when switched back to its original state.

First volunteer images show a large field of view of 50 cm with quite homogeneous image intensity. The add-on system enables 32-channel parallel transmit with 10 µs samples over a large field of view as demonstrated in phantoms and in vivo.

References: 1. Orzada S, Maderwald S, Poser BA, Bitz AK, Quick HH, Ladd ME. RF excitation using time interleaved acquisition of modes (TIAMO) to address B1 inhomogeneity in high-field MRI. Magn Reson Med. 2010 Aug;64(2):327-33.
2. Shooshtary S, Gratz M, Ladd M et al. High-Speed RF Modulation System for 32 Parallel Transmission Channels at 7T. Proc. Intl. Soc. ISMRM 2014, p.544.
3. Solbach K, Abuelhaija A, Shooshtary S. Near-Magnet Power Amplifier with Built-In Coil Current Sensing. Proc Intl. Soc ISMRM 2014, p.1287.
4. Orzada S, Bitz AK, Solbach K et al. A Receive Chain Add-On for Implementation of a 32-Channel Integrated Tx/Rx Body Coil and Use of Local Receive Arrays at 7 Tesla. Proc. Intl. Soc. ISMRM 2015, p.3134.
5. Orzada S, Bitz AK, Kraff O et al. A 32-Channel Integrated Body Coil for 7 Tesla Whole-Body Imaging. Proc. Intl. Soc. ISMRM 2016, p.167.

The research leading to these results has received funding from the European Research Council under the European Union's Seventh Framework Programme (FP/2007-2013) / ERC Grant Agreement n. 291903 MRexcite.

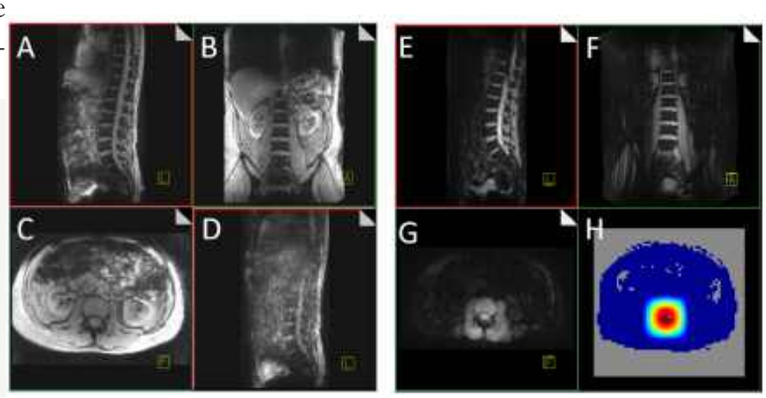

Figure 5: A-C) sagittal, coronal, and axial slice, respectively, from 3D gradient echo sequence acquired with TIAMO during breath-hold. D) Sagittal image from the same 3D sequence acquired during free breathing. Please note the motion artifacts. E-G) 3D gradient echo sequence acquired in free breathing with selective excitation of the spinal column. Sagittal, coronal, and axial slice, respectively. Please note that motion artifacts are largely eliminated. H) Target for the pulse calculation.

R2* relaxation rates of pelvic lymph nodes in USPIO-enhanced MRI of rectal cancer patients at 3 and 7T

In management of rectal cancer, lymph node staging determines treatment regimens and has prognostic implications. In order to optimize non-invasive nodal staging, ultrasmall particles of iron oxide (USPIO)-enhanced MRI could aid in the detection of metastatic lymph nodes, as several studies in prostate cancer have shown (1, 2). The feasibility of the use of USPIO-enhanced lymph node imaging at 7T MR imaging has been studied before (3). USPIO nanoparticles, administered intravenously one day before MR imaging, accumulate through macrophages in healthy lymph nodes. The presence of paramagnetic iron oxide particles locally disturbs the magnetic field homogeneity, causing a rapid signal decay on T2*-weighted imaging. On the contrary, suspicious lymph nodes, presumably without or with less nanoparticles, will retain MR signal.

Figure 1: Axial images of the pelvis of a patient with rectal cancer. In water-excited, T2*weighted images at 3T (A & B) and at 7T (C & D), the same suspicious lymph node can be detected and further analyzed in a ROI (blue) analysis in MevisLab

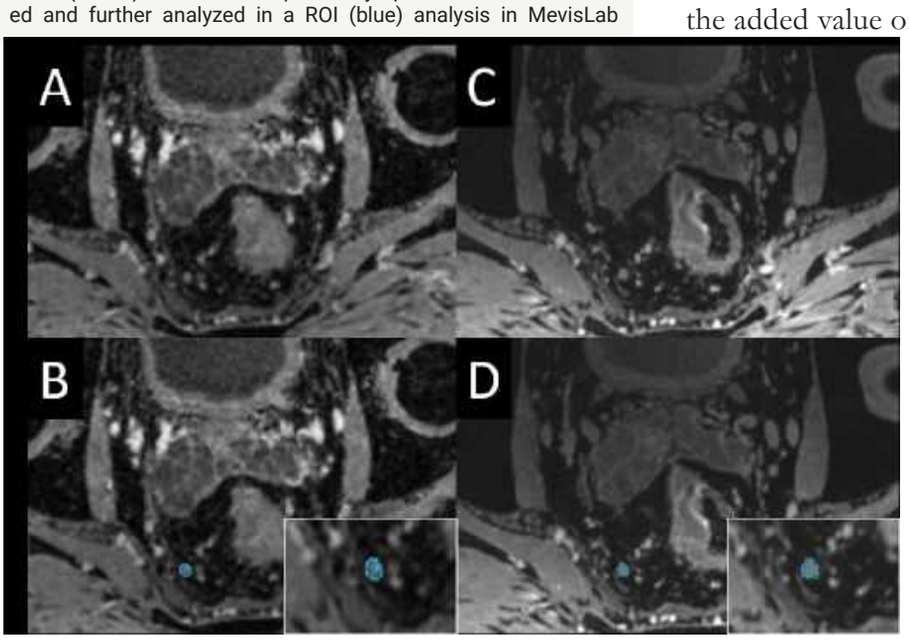

The exact mechanism of nanoparticles accumulation in healthy or partially invaded nodes remains unknown. Therefore, further investigation and comparison between USPIO-enhanced MRI and MRI without USPIO seems to be warranted. To assess the appearance of benign and suspicious lymph nodes we quantified R2* relaxation rates of these nodes in patients with rectal cancer examined both at 3 and 7T. Furthermore, R2* relaxation rates of lymph nodes of rectal cancer patients who did not undergo USPIO infusion, were calculated and compared to the USPIO enhanced suspicious lymph nodes.

Six patients with rectal cancer were examined in a prospective observational pilot study to assess the added value of USPIO-enhanced MR imaging on 3 versus 7T. Five patients with rectal cancer, who did not undergo USPIO infusion, were scanned only at 7T for investigational and comparison purposes. On our 7T system we used the 8/32 channel 1H transceiver body-array coil with meander-type microstrip elements and additional loops (4). After B0 and B1 + shimming, water and lipid selective imaging was performed using the TIAMO technique to obtain homogeneous body imaging (5). Detection of lymph nodes was done on the combination of T1-weighted MRI and water-excited T2*-weighted MRI with multiple gradient echoes and one reconstructed computed echo time of 12msec. All MR images were evaluated by two experienced radiologists. Regions of interest (ROI) were drawn around all annotated lymph nodes using MevisLab (fig 1). The mean signal intensities of lymph nodes per echo time were used to calculate R2* relaxation rates of the nodes at both field strengths

Tijmen Koëter, Rutger Stijns, Bart Philips, Jurgen Futterer, Patrik Zamecnik, Sjaak van Asten, Marnix Maas, Tom Scheenen

Mean and median R2* relaxation rates of the lymph nodes at 3T were 0.14 and 0.11 ms-1 (corresponding to a T2* of 7.1 ms). For the same (paired) lymph nodes at 7T mean and median R2* relaxation rates were 0.21 and 0.15 ms-1 (corresponding to a T2* of 4.8 ms) (fig 2). Mean R2* SD = 0.05) and non-USPIO lymph nodes at 7T (mean R2* = 0.13 ms-1, SD = 0.1), p = 0.004 (fig 3).

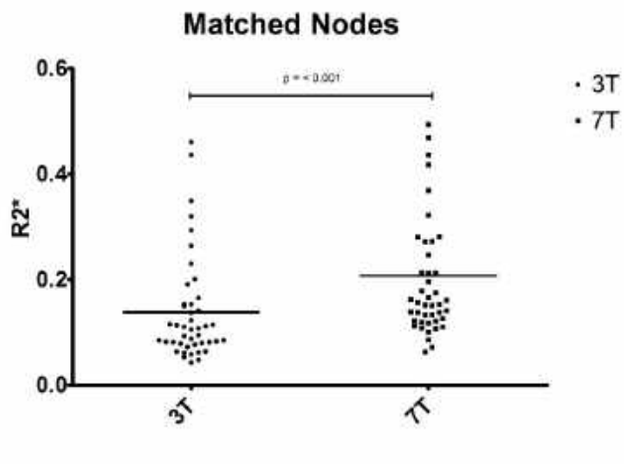

Figure 2: R2 * relaxation rates of matched lymph nodes on 3 and 7T imaging

In the USPIO enhanced lymph nodes, R2* relaxation rates in general appeared to be shorter on 3T compared to 7T. As expected, the suspicious USPIO nodes have shorter R2* rates compared to the nodes with attenuated signal that appeared to be benign. The suspicious USPIO nodes, which are presumed to not contain any iron oxide nanoparticles, however had significant different R2* relaxation rates compared to similar nodes in different patients without USPIO infusion. This points to the presence of USPIO nanoparticles even in suspicious lymph nodes in USPIO-enhanced MRI, so the exact mechanism of USPIO uptake in pararectal lymph nodes remains to be elucidated.

Figure 3: mean R2* relaxation rates of suspicious and unsuspicious lymph nodes at USPIO-enhanced MRI at 7T vs. similar lymph nodes of different patients without any USPIO administration at 7T.

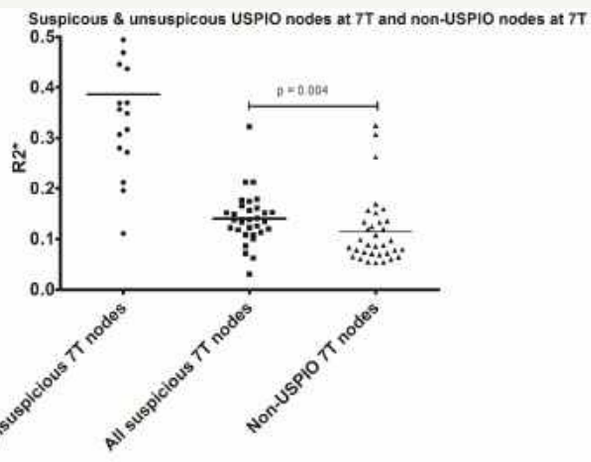

References: 1.Harisinghani MG, Barentsz J, Hahn PF, Deserno WM, Tabatabaei S, van de Kaa CH, et al. Noninvasive detection of clinically occult lymph-node metastases in prostate cancer. N Engl J Med. 2003;348(25):2491-9. 2. Heesakkers RA, Hovels AM, Jager GJ, van den Bosch HC, Witjes JA, Raat HP, et al. MRI with a lymph-node-specific contrast agent as an alternative to CT scan and lymph-node dissection in patients with prostate cancer: a prospective multicohort study. Lancet Oncol. 2008;9(9):850-6. 3. Philips BWJ, Stijns RCH, Rietsch SHG, Brunheim S, Barentsz JO, Fortuin AS, et al. USPIO-enhanced MRI of pelvic lymph nodes at 7-T: preliminary experience. Eur Radiol. 2019. 4. Rietsch SHG, Orzada S, Maderwald S, Brunheim S, Philips BWJ, Scheenen TWJ, Ladd ME, Quick HH. 7T ultra-high field body MR imaging with an 8-channel transmit/32-channel receive radiofrequency coil array. Med Phys. 2018;45(7):2978-2990 5: Orzada S, Maderwald S, Poser BA, Bitz AK, Quick HH, Ladd ME. RF excitation using time interleaved acquisition of modes (TIAMO) to address B1 inhomogeneity in high-field MRI. Magn Reson Med. 2010;64(2):327-33.

T2-prepared multi-echo FLASH for laminar fMRI

The Emmy-Noether funded research group of Dr. Koopmans is interested in methodical developments to improve high resolution raw data acquisition and data analysis techniques for laminar functional magnetic resonance imaging (fMRI). Highfield systems, such as the 7T scanner at the Erwin L. Hahn Institute, deliver the signal-to-noise ratio needed to push the temporal and spatial resolution to an extent acceptable for layer resolved fMRI.

One goal of high resolution fMRI is to examine signal changes at the level of cortical laminae. These are grouped into six histological layers at the cortical surface and tend to have a stereotype behavior in the organization of signal transduction. Therefore, imaging the brain at a sub-millimeter resolution with fMRI techniques provides unique insights into the directionality of information processing in the brain[1].

The majority of fMRI studies use T_2*-weighted echo-planar imaging (EPI) to be as sensitive as possible to the subtle signal changes induced by functional activity. However, at a laminar scale, T_2*-weighting induces a systematic bias toward the pial surface when examining signal changes as a function of cortical depth. Since the underlying contrast mechanism of fMRI is driven by changes in blood susceptibility due to increased cerebral blood flow, the bias is caused by extravascular (EV) effects of large veins. Those dephasing effects can be minimized in a spin echo (SE) experiment which promises higher specificity to signal changes near the origin of neural activity.

T_2-prepared sequences[2] have recently been proposed as an alternative for SE-EPI to perform T_2-weighting with the aim to reduce problems associated with EPI and to reduce unwanted T_2' weighting, which is detrimental for the effective resolution of laminar fMRI as it enhances sensitivity to draining vein effects. We modified a T_2-prepared sequence for laminar fMRI application and performed a multi-echo laminar fMRI study targeting primary visual cortex at 7 T. By varying both SE and gradient echo (GRE) echo times, we investigated contributions from EV effects and potential intravascular (IV) effects of not sufficiently attenuated venous blood to the shape of laminar profiles.

Fig. 1. T_2-prep sequence. (a) Schematic of the sequence. The used T_2-prep module consists of a 90°x hardpulse followed by two adiabatic Gaussian 180°y pulses. The echo at TE_{prep} is brought back to the longitudinal axis with a broadband 90°-x pulse while simultaneously excite the fat signal. Unwanted transverse magnetization is spoiled prior to a multi-echo 3D FLASH

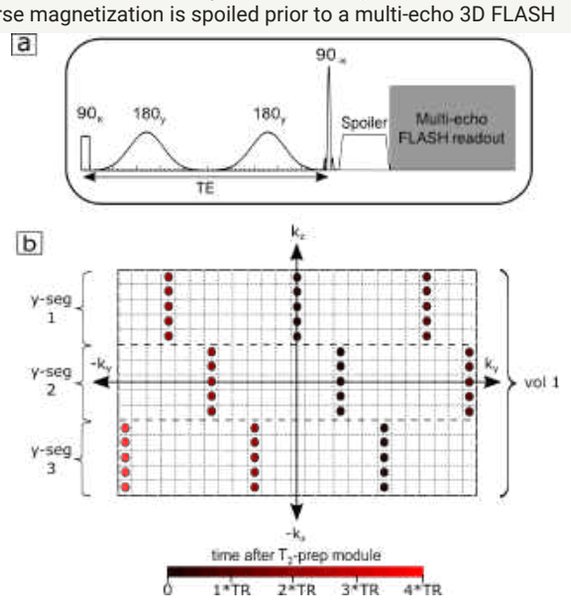

A schematic of the used sequence is shown in Fig. 1 a. The T_2-prep module consisted of a 90°x hard pulse followed by two 180°y adiabatic Gaussian pulses3. A broadband 90°-x sinc pulse was used to flip the spin echo back to the longitudinal axis. The T_2-weighted longitudinal magnetization (Mz) was read out using a multi-echo 3D FLASH sequence. A 252 x 252 x 32 matrix was acquired with an isotropic resolution of 0.75 mm[3]. Functional data at three different spin echo times (TE_{prep}) of 31 ms, 50 ms and 70 ms were acquired in individual runs on different days in one subject. For reproducibility purposes, the scan at TE_{prep} = 31 ms was repeated on another day. For each functional run, four gradient echoes were acquired at echo times (TE_{GRE}) ranging from 2.25 ms to 11.94 ms. Echo spacing was 3.23 ms, TR was 15.2 ms for all $TE_{prep.}$ To reduce unwanted T1-relaxation which would result in a loss of T2-contrast along the long readout, the primary phase encoding

direction ($PE_{y)}$ was 9-fold undersampled, both phase encoding dimension were segmented and the acquisition scheme was center-out. The undersampled data were 3-fold segmented along PE_y and the segments were shifted with respect to each other to create an effective 3-fold untersampling pattern, as shown in Fig. 1 b. The partition encoding direction was 32-fold segmented. With these steps, the effective volume TR was 48.12 s, 49.92 s and 51.84 s for the respective TE_{prep} and the time between two consecutive T_2-prep modules was 501.3 ms, 520 ms, and 540 ms, respectively. Structural data (MPRAGE) were processed in FreeSurfer to be able to perform cortical depth sampling in the functional data. Standard fMRI processing steps (registration, temporal filtering, etc.) were carried out using SPM12. We used the multi-echo T_{EGRE} data to fit a monoexponential decay function to both conditions separately in order to extrapolate to a TE_{GRE} = 0 ms case which hypothetically exhibits 'pure' SE characteristics.

The laminar profiles of relative functional signal change are shown in Fig. 2. For all TE_{prep}, the measured profiles exhibit a strong TEGRE dependency at the boundary of gray matter (GM) and cerebrospinal fluid (CSF) indicated by a linear increase in relative functional signal change with TE_{GRE} (red arrows). This can be explained by either a strong EV effect of pial veins on the superficial layers, an EV effect in CSF which is visible due to partial voluming or a mixture of both. The conclusion that an EV effect in CSF is contributing is supported by the fitted profiles (blue curves in Fig. 2) approaching zero in CSF for TE_{acq} = 0 ms i.e. no EV effect around large vessels for pure SE signal changes.

Deep in GM, the dependency on TE_{GRE} changes when increasing $TE_{prep.}$ At TE_{prep} = 31 ms, the signal change increases with TE_{GRE} in deep layers (black arrows in Fig. 2 a and b). This behavior tends to decrease with increasing TE_{prep} (black arrows in Fig. 2 c and d). Giving a T_2* of GM of approximately 28.7 ms at rest and 29.3 ms during activation[4] at 7T, a signal change based on EV T_2* effects around capillaries is approximately constant at the TE_{GRE} used here. An EV effect of pial veins and/or ascending veins would have shown an increase in GM signal change for all TE_{prep} but this is absent. Instead, the signal change likely stems from a not completely decayed intravascular component at low TEprep, blurring the profiles by following the increase of baseline CBV from deep to superficial layers (Fig. 2 a and b). With increased TE_{prep}, the contribution from this component is reduced. The fitted curves tend to underline this explanation i.e. the bias towards the GM/CSF boundary is reduced with increasing TE_{prep}.

The results suggest that intravascular signal change contributions are present in T_2-prep FLASH data at low TE_{prep}, probably due to not fully decayed blood signal. In ascending veins, this results in blurring of laminar profiles. Effectively nulling the blood compartment circumvents this issue. Without too excessive additional T_2'-weighting, T_2-prep effectively reduces EV contributions from large veins resulting in desired T_2-weighted signal changes. Future work can elaborate on the partial voluming effect with CSF by using asymmetric voxel sizes[5]

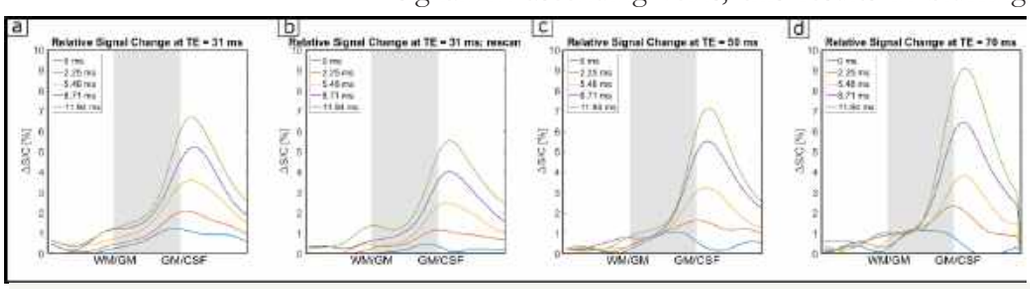

Fig. 2. Laminar Profiles. Relative functional signal change as a function of cortical depth, TE_{GRE} and TE_{prep}. For all TE_{prep}, strong EV effects are visible at the pial surface (red arrows) which are absent for the extrapolated TE_{GRE} = 0 ms profiles (blue lines in e.g. c and d). Deep in GM (black arrows), a TE_{prep} of 31 ms is not long enough to effectively suppress IV signal changes resulting in an increase in signal change upon TE_{GRE} variation (a and b). Longer TEprep do not exhibit this effect (c and d). Without too excessive T2'-weighting, T2-prep multi-echo FLASH imaging results in the desired T2-weighted signal changes.

References: 1.Lawrence et al. NeuroImage 2017; 197:785-791. 2. Hua et al. MRM 2014; 72:1530-1540. 3. Tannús et al. NMR Biomed 1997; 10:423-434. 4. Uludag et al. NeuroImage 2009; 48:150-165. 5. Kashyap et al. Sci. Rep.

The research leading to these results has received funding from the DFG grant KO5341/1 1.

Involvement of the Cerebellum in Emotional Learning

In our understanding of the brain, the role of the cerebellum is mainly associated with motor functions. It has been found, however, that patients suffering from cerebellar diseases not only display motor deficits, but also cognitive and emotional abnormalities. Furthermore, there is initial evidence that the cerebellum serves as a predictive device not only in the motor but also in the cognitive domain (Sokolov, Miall et al. 2017). The aim of the present study was to show that this is equally the case in the emotional domain. The basic idea of this predictive function is, that an internal model is used to compute a prediction of a likely outcome of an event or action. Differences between the prediction and the actual (in the case of movements sensory) outcome, i.e. prediction errors, are in turn used to update the internal model, and hence to adapt for changing inner and outer environmental conditions. We studied fear conditioning as an example of learning in the emotional domain.

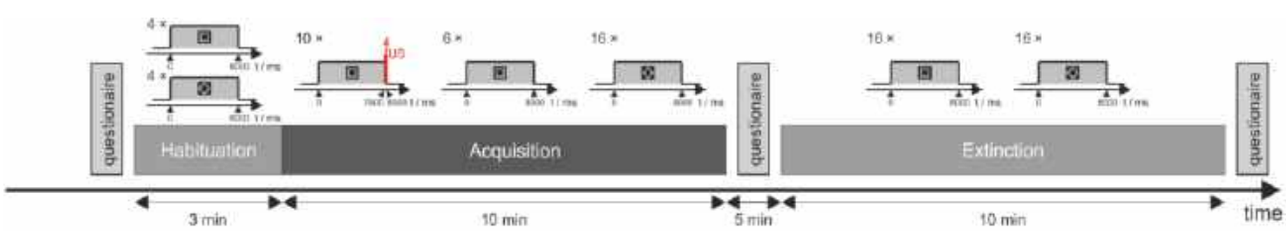

Figure 1: Schematic experimental paradigm for fear conditioning experiment. US (aversive electric shock) is only applied in acquistion phase, when 8 seconds of CS (square or diamond picture) presentation is followed by an US in 10 out of 16 CS+ cases, and never in case of CS-. Use of CS images was counterbalanced for the entire test group.

Fig. 1: Schematic diagram of the experimental paradigm. US (100 ms aversive electric shock) was applied in acquisition phase. Eight seconds of CS presentation (square or diamond shape) were followed by an US in 10 out of 16 cases for CS+ and never for CS-.

A differential, delay fear conditioning paradigm was investigated in 27 young and healthy human subjects in the 7 T magnetic resonance (MR) scanner at the Erwin L. Hahn institute. Twentytwo participants (14 females, mean age 26.9 years, range: 19 to 32 years) were included in the final analysis. The experiment was performed within one session inside the MRI scanner. Two visual stimuli were used as conditioned stimuli (CS), and an unpleasant, but not painful electrical shock as unconditioned stimulus (US) (Fig. 1). The US was applied to the palm of the left hand. Skin conductance (SCR) was measured as behavioral parameter, and arousal and valence were assessed using questionnaires. Ratings and SCR were evaluated using MATLAB (The MathWorks Inc., MA) and SPSS (IBM Corp., NY). MRI data was acquired using a 32-ch head coil (Nova Medical, MA). Anatomic reference was acquired using MP2RAGE sequence at 0.75 mm isotropic resolution. Whole brain fMRI acquisition was performed using a 2D simultaneous multi-slice (SMS)-EPI sequence at 1.7 mm isotropic resolution. Image analysis was performed using mainly SPM12. Analysis was performed on cerebellum-normalized data using the SUIT toolbox for SPM (Diedrichsen 2006). First level analysis was modeled for the whole experiment using realignment parameters and pulse-oximetry/respiration-belt based RETROICOR method for nuisance regressors. CS-events, US events and omission of US events (no-US events) were modeled. For explorative evaluation all regressors of interest were used for a within-subject ANOVA spanning the entire experiment. For post-hoc tests appropriate first level contrasts were generated and tested in second level t-tests.

Skin conductance responses (SCR), as well as (hedonic) valence and (emotional) arousal ratings documented successful conditioned fear acquisition

Thomas M. Ernst, G Giorgi Batsikadze, Anna Brol, Marcel Gratz, Christoph Ritter, Ulrike Bingel, Marc Schlamann, Stefan Maderwald, Harald H. Quick, Christian J. Merz , Dagmar Timmann

and extinction in the 7 T scanner environment (e.g. SCR, 2nd half of acq.-phase, CS+>CS-, $t(21)=2.37$, $p<0.027$) (Fig. 2b). As expected, functional MRI analysis revealed widespread cerebellar activation related to the presentation of the US (Fig. 2c). In the acquisition phase, bilateral activation was observed in CrusI/Lob.VI

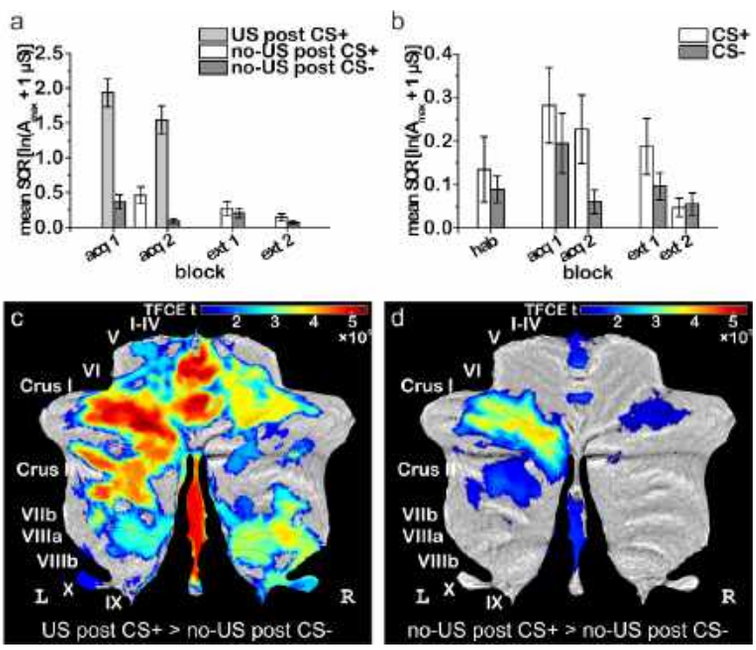

Fig. 2: Skin conductance responses (a) related to US and US omission, and (b) CS presentation; cerebellar fMRI activation (c) related to the presentation of the US, and (d) related to the unexpected US-omission.

related to the prediction of the US in CS+ trials, and, most importantly, more pronounced activations related to the US omission in CS + (Fig. 2d).

Cerebellar activation was observed related to the learned association of the CS and the aversive US confirming previous results (Sacchetti, Baldi et al. 2002). Most importantly, marked cerebellar activation was found also during the unexpected omission of the unpleasant event and disappeared during extinction trials (in which the omission became expected). Prediction errors are thought to drive associative fear learning. Previous studies focused on the role of the amygdala, insula, midbrain periaqueductal gray and striatum. Thus, our findings provide evidence that the cerebellum is part of a more extended neural network processing prediction errors underlying emotional associative learning. At the same time, our findings add to the assumption that the cerebellum performs one single neural operation that is acting as a predictive device. Data has been published in Ernst et al. (2019).

References: 1.Diedrichsen, J. (2006). "A spatially unbiased atlas template of the human cerebellum." Neuroimage 33(1): 127-138.
2. Ernst, T. M., A. E. Brol, M. Gratz, C. Ritter, U. Bingel, M. Schlamann, S. Maderwald, H. H. Quick, C. J. Merz and D. Timmann (2019). "The cerebellum is involved in processing of predictions and prediction errors in a fear conditioning paradigm." Elife 8.
3. Sacchetti, B., E. Baldi, C. A. Lorenzini and C. Bucherelli (2002). "Cerebellar role in fear-conditioning consolidation." Proc Natl Acad Sci U S A 99(12): 8406-8411.
4. Sokolov, A. A., R. C. Miall and R. B. Ivry (2017). "The cerebellum: adaptive prediction for movement and cognition." Trends Cogn Sci 21(5): 313-332.

Funded by the Collaborative Research Center 316803389 (SFB1280 Extinction Learning, Projects A05, A09, A11).

The traveling heads 2.0: Reproducibility of Quantitative Imaging Methods at 7 Tesla

The "traveling heads" is an experiment originally started in 20141 to assess the comparability and reproducibility of multicenter human brain imaging with the focus on qualitative and structural measurements performed at 7T. The current follow-up study now evaluates the precision of state-of-the-art quantitative imaging methods at 7T, again with a focus on reproducibility for multicenter trials. Two subjects, termed the "traveling heads", were measured multiple times at 10 different 7T MR systems within the German Ultra-high Field Imaging (GUFI) network. The sites include different generations of 7T MR systems to assess not only inter- and intra-site but furthermore cross-generation reproducibility; the systems include the older installed base (since 2004) and the most recent generation of FDA-approved 7T MR systems (since 2017).

The study includes the analysis on the reproducibility of MP2RAGE-based measurements, QSM, CEST, and relaxometry based on a multi-echo FLASH sequence. System calibration was also monitored to assess the influence of system calibration methods on quantification. We imaged two male subjects (41 and 36 yrs.) at ten UHF sites of the GUFI network. All those sites operate a 7T whole-body MR system from the same vendor (Siemens Healthcare, Germany). The systems represent different generations of 7T with five different hard- and software configurations (Fig. 1).

Configuration Type	Magnet type	Gradient Coil	RF Coil	Software Version	Location (Scans)
1 (PS, AS95, 24ch)	Passively shielded	38 mT/m	24 ch	VB	Berlin (1) Heidelberg (1)
2 (PS, AS95)	Passively shielded	38 mT/m	32 ch	VB	Essen (2)
3 (PS, SC72)	Passively shielded	70 mT/m	32 ch	VB	Magdeburg (1) Leipzig (1) Vienna (1)
4 (AS, SC72)	Actively shielded	70 mT/m	32 ch	VB	Bonn (1)
5 „Terra"	Actively shielded	80 mT/m	32 ch	VE	Erlangen (3) Würzburg (2) Jülich (1.5)

Imaging Protocol	
B1 mapping	DREAM, 5 mm iso, TA: 0:05 min
B0 mapping	Double Echo GRE, 3 mm iso, TA: 2min
Volumetry	MP2RAGE, TR: 6000 ms, TI: 800/2700 ms, TE: 3.0 ms, 0.75×0.75×0.75 mm³ TA: 9:38 min
QSM	ME GRE, 0.7×0.7×0.7 mm³ TA: 9:50 min
Relaxometry	2x ME Flash 3D, pd- and t1-weighted, 0.7×0.7×0.7 mm³ 2x TA: 9:41 min
CEST	3D CEST, 1.72x1.72x3 mm³, 54 offsets, 140 Gaussian-shaped pulses, TA: 13 min

Figure 1: Sites and measurements of the study. All 7T MR systems are from the same vendor. Configurations 1-4 use magnets manufactured by Agilent (UK); configuration 5 by Siemens. All sites are equipped with a commercially available RF head coil (Nova Medical) The current version has 32 and the older version has 24 receive channels. The imaging protocol was designed to use the same or most similar sequences and parameters at all sites implemented at both software versions

The **system calibration** procedures were monitored with B1 and B0 mapping techniques. For B1 we used DREAM2 B1 mapping for adjusting and mapping. B0 was shimmed iteratively using automatic shimming routines. The "Terra" sites had 3rd-order shimming enabled, while at the other sites 2nd-order shimming was used.

The DREAM B1 adjustment was successfully applied and gave us a mean flip angle of 92% of the nominal flip for the whole brain volume, and 96% in supratentorial brain between all measurements. Variations were small between sites (+-4%) and subjects (<2%). The transmit power at the 24ch coil sites was fixed to 350V. Since this coil type was less power efficient and SAR constraints of other measurements in our imaging protocol limited the maximum applicable input power. This led to lower B1 values (84%/86% whole brain:WB/ supratentorial brain:SB). In contrast, the B0 shimming performed slightly better at the 24ch coil sites, with a 5% (WB and SB) lower standard deviation of the field map compared to the 32ch coil sites.

Volumetric measurements were done with MP2RAGE image data. The "uniform"-MP2RAGE images and T1-maps (Fig. 2) were B1-corrected.[3] Subsequently bias correction, brain extraction and arteries filtering, tissue segmentation and segmentation of different subcortical structures were calculated to gain different brain masks for analysis of all image data via co-registration between measurements. **MP2RAGE** showed very high agreement in image contrast, measured T1 values and volumetric measurements (Fig. 2). The quantitative measurements were highly comparable to previous traveling heads measurements.[1]

Maximilian N. Völker, Oliver Kraff, Steffen Görke, Frederik B Laun, Jannis Hanspach, Kerrin J. Pine, Philipp Ehses, Moritz Zaiss, Andrzej Liebert, Sina Straub, Korbinian Eckstein, Simon Robinson, Armin N. Nagel, Maria R. Stefanescu, Astrid Wollrab, Sabrina Klix, Jörg Felder, Michael Hock, Oliver Speck, Mark E. Ladd and Harald H. Quick

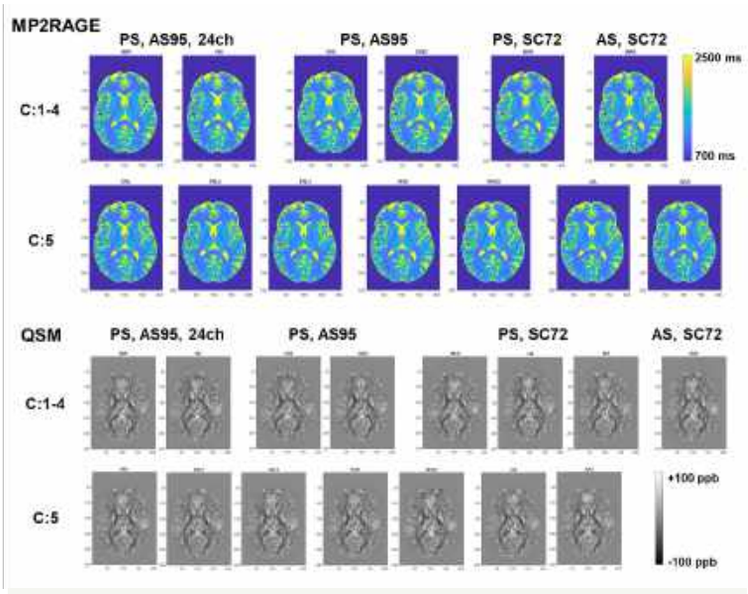

Figure2: MP2RAGE T1 maps obtained via combination of both inversion contrasts. Site data is ordered depending on the system configuration C (Fig.1).All data were co-registered to C2:ESS. T1 maps show very high agreement between the different sites- QSM maps show very similar contrast but small artifacts are visible for example in median regions like the cor-

QSM was acquired using a multi-echo GRE sequence with ASPIRE[4] phase reconstruction and QSM maps were calculated using Laplacian-based phase unwrapping, background field removal, STAR-QSM reconstruction[5] and echo-time averaging. A brain mask was generated at one site for each subject and co-registered to all sites to include the same brain volume at each site for calculation and normalization. **The QSM-maps** also showed a very high qualitative agreement between sites (Fig. 2). Quantification of distinct subcortical gray matter VOIs yielded a slightly higher variation between sites (e.g. 8%/6% for left pallidus of subject 1/2). **CEST-MRI** was realized according to a previously optimized acquisition protocol at 7T[6] where the image readout was extended to three dimensions using the snapshot-CEST approach[7]. Z-spectra were de-noised using a principal component analysis and the final CEST contrasts were calculated by the inverse metric. The **CEST** analysis of the rNOE-maps showed high agreement between the "Terra" sites alone as well as between the non-Terra sites alone, but not across all system generations. For the "Terra" sites higher transfer rates were measured. This may be explained by differences in the implementation of the sequence at different software version leading to a slightly different readout leading to T2* effects which may have been measured. Quantitative maps of **R1, R2* and PD** were acquired a multi-parametric mapping technique[8] further adapted for 7T and for increased isotropic resolution. The Maps were calculated with the hMRI toolbox (http://hmri.info). Multi-parametric mapping with ME-GRE showed very good agreement between sites with a slightly higher variation at subject 1 data (6%/5% for T1, 8%/4% for T2* and 3%/1% for PD of left pallidus for subject 1/2). Subject 1 had a 24% higher whole brain standard deviation of the shimmed B0 field than subject 2.

Quantitative imaging is challenging at UHF, as these methods are very sensitive but not yet standardized. Individual UHF systems, even from the same vendor, have differences in hardware and software that might potentially influence quantification of image data. Our data showed that harmonized state-of-the-art quantitative imaging methods between different UHF sites and scanner architectures, even across nearly 15 years of operation, lead to a very high reproducibility for inter-site comparisons in the same subjects. Some differences occurred especially where different platforms/software versions or different RF coils were used. Therefore, special care has to be taken in multicenter studies if the detectable effect is in the order of the variation we found in this study.

References: 1.Voelker MN et al. The traveling heads: multicentre brain imaging at 7 Tesla, MAGMA. 2016;29(3):399-415) 2. Ehses P. et al Whole-brain B1 -mapping using three-dimensional DREAM. Magn Reson Med. 2019 Sep;82(3):924-934. 3. Marques JP et al. (2013). New developments and applications of the MP2RAGE sequence–focusing the contrast and high spatial resolution R1 mapping. PLoS One, 8(7). 4. Eckstein K et al. Computationally Efficient Combination of Multi-channel Phase Data From Multi-echo Acquisitions (ASPIRE). Magn Reson Med. 2018 Jun;79(6):2996-3006. doi: 10.1002/mrm.26963. Epub 2017 Oct 16. 5. Wei H et al. „Streaking Artifact Reduction for Quantitative Susceptibility Mapping of Sources with Large Dynamic Range", NMR in Biomedicine (10), 1294–1303 (2015). 6. Zaiss M et al. Relaxation-compensated CEST-MRI of the human brain at 7 T: Unbiased insight into NOE and amide signal changes in human glioblastoma. NeuroImage 2015; 112:180-188 7. Zaiss M et al. Snapshot-CEST: Optimizing spiral-centric-reordered gradient echo acquisition for fast and robust 3D CEST MRI at 9.4 T. NMR Biomed 2018; 31:e3879 8. Weiskopf N et al. Quantitative multi-parameter mapping of R1, PD(*), MT, and R2(*) at 3T: a multi-center validation. Front Neu-

This work was supported by a grant from the German Research Foundation (DFG)/projectGermanUltrahighFieldImaging/Grantn.LA1325/7-1,QU154/5-1. UHF-adapted imaging sequences were provided by Siemens Healthcare.

Dissociable laminar profiles of concurrent bottom-up and top-down modulation in the human visual cortex

Using 'ultra-high field' MRI systems of 7T and above, it has become possible to non-invasively measure fMRI responses at sub-millimetre resolution, allowing us to perform lamina-resolved brain activation studies in humans examining the fine structure of the grey matter. This has allowed researchers to ask new questions about the functional organization of the human brain, and examine communication between brain areas in more detail than previously possible. One important promise of laminar fMRI is its potential ability to distinguish between bottom-up and top-down BOLD responses. While these are spatially amalgamated at standard imaging resolutions, they are expected to be expressed at different cortical depths. Bottom-up connections between brain areas are known to target the granular layer 4, at middle cortical depths, while top-down connections target deeper and superficial layers but largely avoid layer 4. It should therefore be possible to tease apart the bottom-up and top-down contributions by examining that response across cortical depth. Here we measured lamina-resolved fMRI responses from participants as they viewed visual stimuli and were required to attend to a specific stimulus feature (orientation). Our stimulus paradigm was designed to elicit concurrent bottom-up and top-down modulations of the stimulus-driven response through orthogonal manipulations of stimulus contrast (bottom-up) and feature-based attention (top-down), both of which are known to influence early visual cortex responses (see figure 1). We predicted that response modulations driven by attention would operate at different cortical depths to those driven by changes in stimulus contrast. Specifically, contrast modulations were expected to be largest at middle cortical depths, as increases in contrast should be associated with stronger bottom-up input to the granular layer. Top-down influences are generally expected to be strongest in the deep and/or superficial cortical depths (agranular layers) Twenty-six healthy participants completed the experiment. Functional data were acquired with a T2*-weighted 3D gradient-echo EPI sequence (TR 3408 ms, TE 28 ms, 0.8 mm isotropic voxels, 16° flip angle, 192 x 192 x 38.4 mm field of view, GRAPPA acceleration factor 4). Laminar-specific time courses were estimated separately for the different orientation-preferring voxel populations from visual areas 1-3 combined to examine overall laminar activity across the visual cortex.

As expected, BOLD responses in early visual cortex were modulated by both subjects' attention towards a specific orientation and changes in stimulus contrast. Responses to high contrast stimuli were significantly higher than low contrast stimuli.Voxel responses were also higher when their

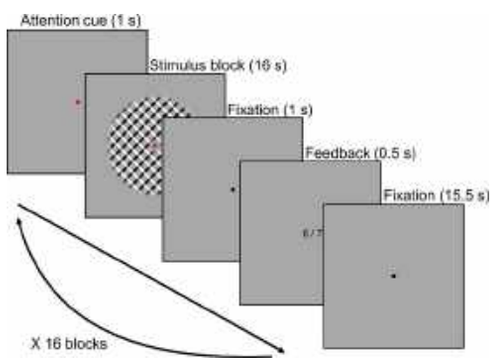

Figure 1: Task design. Plaid stimuli were presented in a block design. During stimulus blocks, eight stimuli were presented. Subjects were required to respond to each stimulus (except for the first in each block), indicating whether the bars in the cued orientation were thicker or thinner compared to the previously presented stimulus. Attention was cued by the coloured fixation dot: red, attend to orientation shown by black bars in figure, green, attend to white. Stimulus blocks were preceded by an attention cue and followed by performance feedback and an inter-block interval.

preferred orientation was attended, compared to when the orthogonal orientation was attended. Overall, therefore, our paradigm was successful in inducing strong modulations of stimulus-driven BOLD responses using bottom-up (contrast) and top-down (feature-based attention) task manipulations.

Next, we determined whether the effects of feature-based attention and stimulus contrast on

Samuel J. D. Lawrence, David G. Norris, Floris P. de Lange

BOLD responses varied across cortical depth, and whether they did so differently from each other. We computed separate BOLD time courses specific to three equal volume grey matter depth bins defining deep, middle and superficial cortex. Depth-specific time courses were normalised to remove overall differences in signal intensity between layers Normalised depth-specific time courses were analyzed to compare the laminar profile of activity modulations resulting from top-down attention and bottom-up stimulus contrast. Response modulations from both feature-based attention and stimulus contrast were clearly present in depth-specific time courses (Figure 2 A–D). In order to fairly compare laminar profiles across conditions, we used data from the same time points (highlighted in Figure 2A & C), which comprised the peak of the BOLD response during a block of stimuli and during which both the effects of attention and contrast were significant. Within this time window, the effect of feature-based attention on neural responses was present at all cortical depths and was largest in the superficial layers. There was a trend of activity differences between layers induced by the attentional manipulation. Unpacking this, the attentional modulation was significantly stronger in the superficial layers compared to the middle and deep layers, while there was no significant difference in the strength of the attentional modulation between the deep and middle layers. Modulations from changes in stimulus contrast were organized quite differently, peaking at middle depths (Figure 2D). Indeed, contrast modulations varied significantly across depth, being largest at middle compared to deep and superficial depths. Critically, the organization of contrast-related modulations across depth was significantly different to those caused by feature-based attention. As such, the laminar profiles of responses modulations across the early visual cortex were dependent on whether those modulations were bottom-up or top-down in origin.

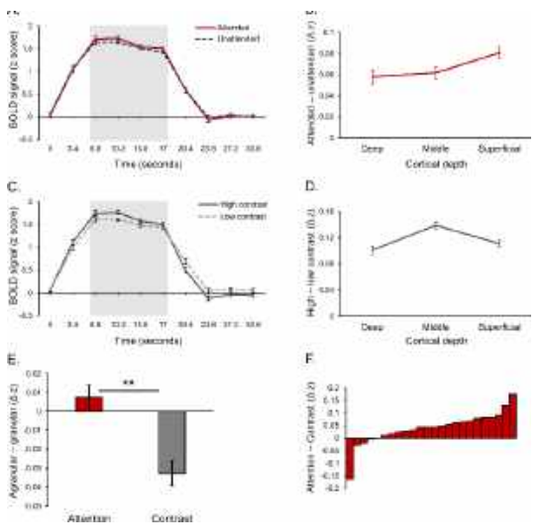

Figure 2: Laminar organization of top-down and bottom-up response modulations in V1-V3 combined. Figures are summarised in the text.

We predicted that top-down effects were more likely to be expressed in agranular layers compared to bottom-up effects. To explicitly test for this, we computed a score that described whether experimental effects were more agranular or granular. This was done by averaging the effect of feature-based attention (or contrast) from the superficial and deep depth bins (agranular) and subtracting that from the middle bin (granular). As such, a positive score indicates a largely agranular effect, while a negative score indicates a granular effect. As predicted, feature-based attention effects were more agranular compared to stimulus contrast (Figure 2E). This difference was significant, and 20 of our 24 subjects showed an effect in this direction (Figure 2F). Therefore, it appears that top-down contributions to response modulations were stronger in the agranular layers compared to bottom-up contributions, which were strongest in the granular layer. As can be seen from Figure 2B, the agranular profile of attention was driven by the fact that the attentional modulation was strongest in the superficial layers.

Our results show clear differences in how bottom-up and top-down aspects of perceptual processing affect brain responses across cortical depth and are consistent with the anatomical organisation of feedforward and feedback connections between brain areas. To our knowledge, our study also provides the first report of how visual cortex responses are modulated by feature-based attention at the laminar level. Most importantly, we demonstrate that laminar fMRI methods can be used to examine both the bottom-up and top-down components of the overall BOLD response as they co-occur during the processing of a stimulus.

Relationship between thrombus and aneurysm wall in partially thrombosed intracranial aneurysms visualized with 7T MPRAGE

Thrombosed intracranial aneurysms are often associated with increased aneurysm wall instability and present a challenge for treatment1. Recently, contrast enhancement in the aneurysm wall of thrombosed ICAs could be visualized in vivo using high-resolution gadolinium-enhanced 7 Tesla (T) magnetic resonance imaging (MRI)2. However, no studies have evaluated the relationship between the thrombus characteristics and the aneurysm wall. This in-vivo study aimed to investigate the relationship between thrombus characteristics and the aneurysm wall in partially thrombosed intracranial aneurysms using MPRAGE at 7T MRI3, 4.

The study cohort included fifteen patients (7 males, 8 females) with sixteen partially thrombosed intracranial aneurysms. All subjects were evaluated utilizing a 7T whole-body MR system (MAGNETOM 7T, Siemens Healthcare GmbH, Erlangen, Germany) equipped with a 1/32-channel Tx/Rx head radiofrequency coil (Nova Medical, Wilmington, USA). The gradient system provides 40 mT/m maximum amplitude and a slew rate of 200 mT/m/ms. A modified MPRAGE sequence was obtained with the following sequence parameters: FOV = 270×236 mm2, matrix = 384×336, resolution = 0.7×0.7 mm 2, slice thickness = 0.7 mm, TR = 2500 ms, TE = 1.54 ms, flip = 7°, BW = 570 Hz/pixel, TA = 6 min 13 sec. The signal intensity ratio in the thrombus was defined as the highest signal intensity in the thrombus divided by the signal intensity in the anterior corpus callosum. The signal intensity ratio in the thrombus was compared to the thickness of the aneurysm wall at 7T MPRAGE. Histopathological findings in six tissue samples were correlated with 7T MRI to identify the microstructures.

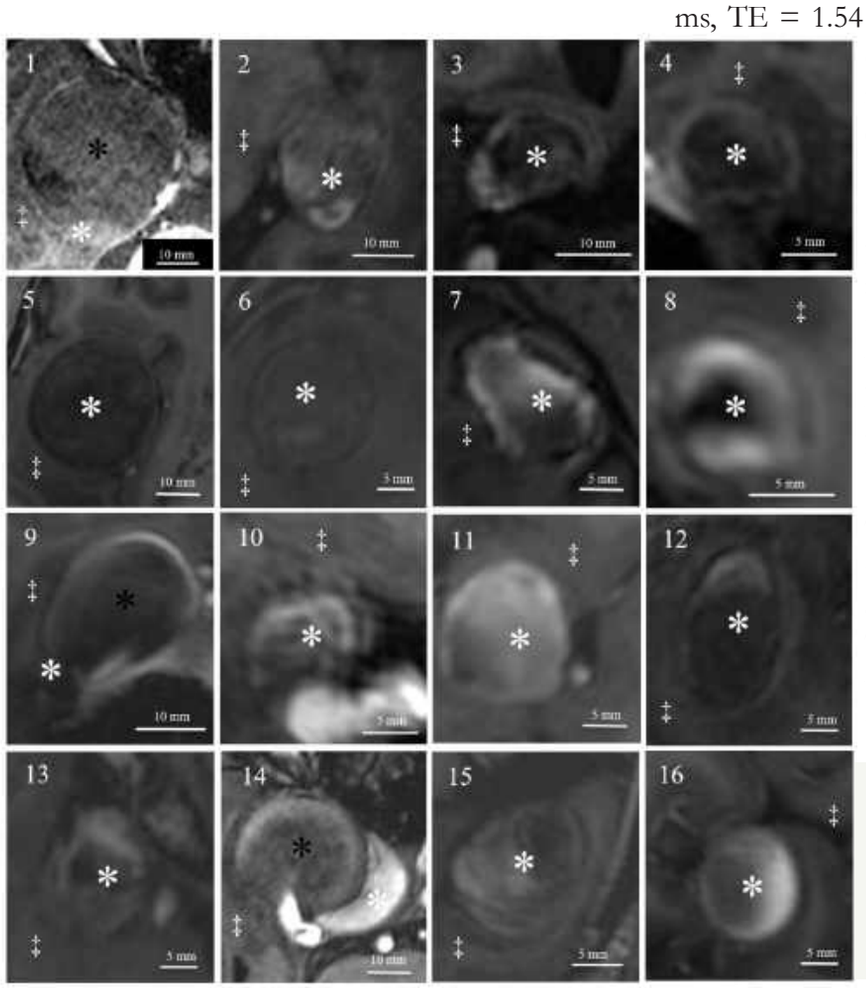

The mean signal intensity ratio of thrombus was 0.97 (standard error of the mean 0.14, range 0.27-2.28). The mean thickness of the aneurysm wall was 1.25 mm (standard error of the mean 0.08, range 0.84-1.55 mm).

Figure 1: . Delineation of thrombosed intracranial aneurysms at 7T MRI. Identical structures are marked in all subfigures as follows. White asterisks: intraluminal thrombus; black asterisks: aneurysm lumen; double daggers: brain parenchyma.were preceded by an attention cue and followed by performance feedback and an inter-block interval.

Bixia Chen, Taku Sato, Toshinori Matsushige, Oliver Gembruch, Michael Forsting, Alexander Radbruch, Jan Rodemerk, Shiqing He, Stefan Maderwald, Harald H. Quick, Mark Ladd, Ulrich Sure, Karsten H. Wrede

The signal intensity ratio ofthrombus significantly correlated with the thickness of the aneurysm wall ($p < 0.01$) as shown in Figure 2. The aneurysm walls with the highest signal intensity ratio of thrombus were significantly thicker. In the histopathological examinations, three cases with hypointensity of the thrombus in MPRAGE showed only a few macrophages in the thrombus and a thin, degenerated aneurysmal wall (not shown). On the other hand, three cases with hyperintensity of the thrombus in the MPRAGE showed abundant macrophages in the thrombus (Figure 3).

In MPRAGE at 7T MRI, the signal intensity ratio of thrombus in partially thrombosed intracranial aneurysms correlates with aneurysm wall thickness and histologic features indicating wall instability.

References: 1.Guresir E, Wispel C, Borger V, et al. Treatment of partially thrombosed intracranial aneurysms: Single-center series and systematic review. World Neurosurg . 2018;118:e834-41 2. Sato T, Matsushige T, Chen B, et al. Wall contrast enhancement of thrombosed intracranial aneurysms at 7t mri. AJNR Am J Neuroradiol. 2019;40:1106-11 3. Wrede KH, Johst S, Dammann P, et al. Caudal image contrast inversion in mprage at 7 tesla: Problem and solution. Acad Radiol. 2012;19:172-78 4. Umutlu L, Theysohn N, Maderwald S, et al. 7 tesla mprage imaging of the intracranial arterial vasculature: Nonenhanced versus contrast-enhanced. Acad Radiol. 2013;20:628-34

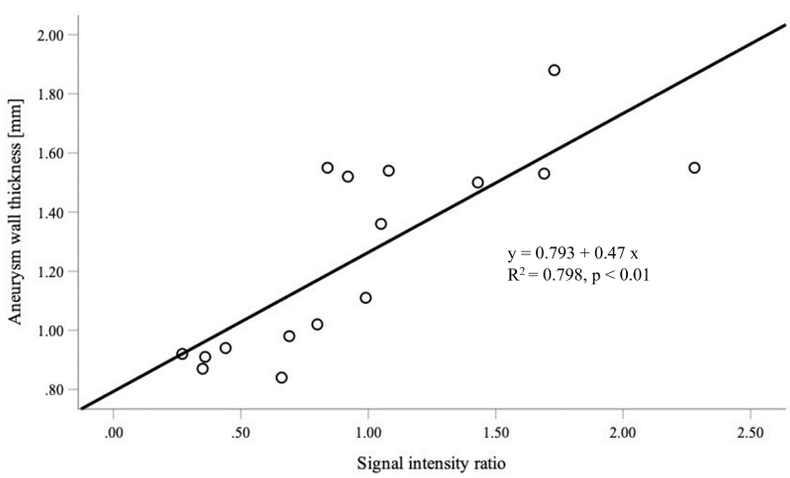

Figure 2: Correlation of signal intensity ratio of the thrombus with aneurysm wall thickness (p<0.01).

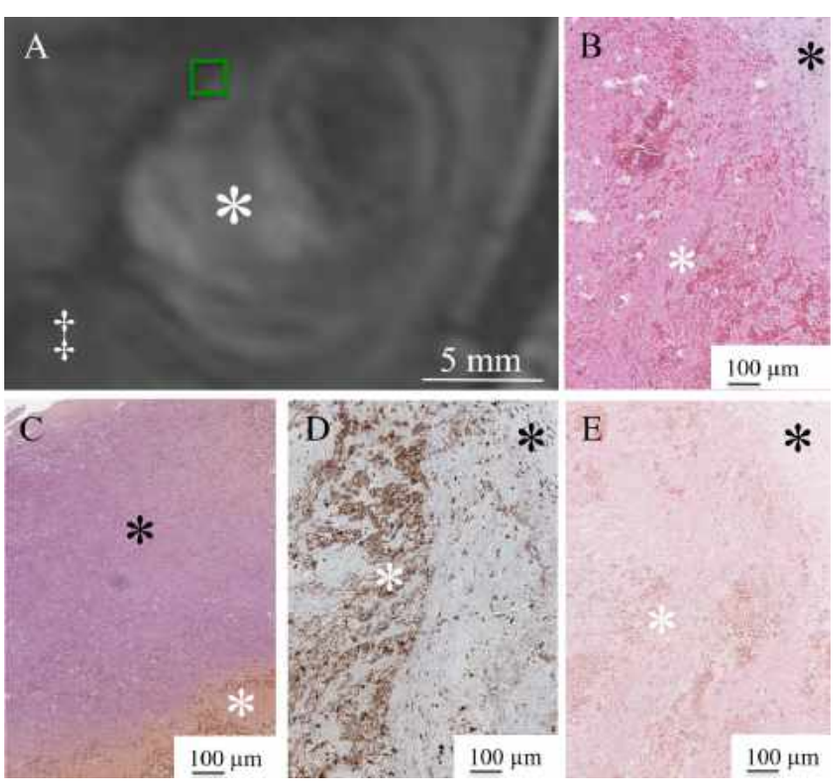

Figure 3:MPRAGE shows high signal intensity pattern in Aneurysm No. 15 (white asterisk: intraluminal thrombus; double daggers: brain parenchyma). Green box indicates area of histopathological specimen (A). White asterisk indicates intraluminal thrombus (B-E). Abundant red blood cells in the thrombus (white asterisk) in HE staining (B). Thick aneurysm wall layer in Verhoeff-Van Gieson staining (black asterisk) (C). Abundant macrophages (white asterisk) in the thrombus in CD68 immunostaining (D). Limited iron deposition (white asterisk) in the thrombus stained with Prussian blue (F).

3T and 7T MR examinations of head trauma in American football players

Preliminary results from a multi-disciplinary pilot trial over the 2019 American football season in Germany

American football players (AFP) experience repetitive brain trauma during their career. While such concussions cause temporal functional disorders of the brain, a variety of concussions can also lead to long-term functional and structural changes in the brain. Subclinical concussions may also cause chronic traumatic encephalopathy (CTE), which is a suspected neurodegenerative disease diagnosed in the brains of former contact and collision athletes. Structural changes in AFP brains, such as the loss of white matter integrity can already be demonstrated after a football season, and also in players with mild skull brain contusions. The level of Tau protein in blood can be determined as a potential biomarker for diffuse axonal injury and blood-brain barrier interruptions, as it correlates with the loss of white matter integrity [1]. Cerebral microbleeds (CM) are a typical finding of repetitive brain trauma and diffuse axonal injury and show a frequency of about 9% in retired AFP [2]. However, only a limited number of studies are available on this topic, and a dedicated study on 7T MRI combined with comparative imaging at 3T as well as neuropsychological and biochemical testing is missing. Ultrahigh field MRI shows significantly more CM in patients with diffuse axonal injury at 7T than at 3T [3]. The purpose of this multi-disciplinary study is to use a broad range of parameters to characterize structural, functional and biochemical brain changes in AFP.

Figure 1: Two AFP in front of the 7T MR system. Imaging was performed without football gear.

A total of 18 male AFP (ages: 18-33 years) were evaluated before and after the 2019 season of the German Football League. A second cohort of 18 gender- and age-matched subjects with no history of contact and collision sports served as a control group. Multi-parametric MR imaging of the brain was performed at two field strengths, i.e. at 3T (MAGNETOM Skyra, Siemens Healthcare GmbH, Germany) with a focus on diffusion tensor imaging as well as in comparison to 7T (MAGNETOM 7T, Siemens Healthcare GmbH, Germany) which focused on volumetry and high-resolution (quantitative) susceptibility weighted imaging (QSM, SWI). Both MR systems were used in combination with 32-channel radiofrequency head coils. Image analyses were performed by two neuroradiologist in consensus reading on 3T MRI and on 7T MRI for number of CM and additional findings. In addition, neuropsychological test procedures were used to examine cognitive and emotional performance and to assess the depression status of each subject. Blood samples were examined for various biomarkers.

The preliminary results showed a total of three CM in the pre-season images in three different AFP in the 3T SWI (Figure 1). In the 7T SWI one of these CM was confirmed (Figure 1B), moreover even two smaller adjacent CM were identified. The other two suspected CM at 3T in the other two AFP were identified at 7T as atypical small

Oliver Kraff, Cornelius Deuschl, Janis Evers, Christiane Oedekoven, Theres Bastgen, Alexander Radbruch, Michael Forsting, Richard Dodel, Harald H. Quick

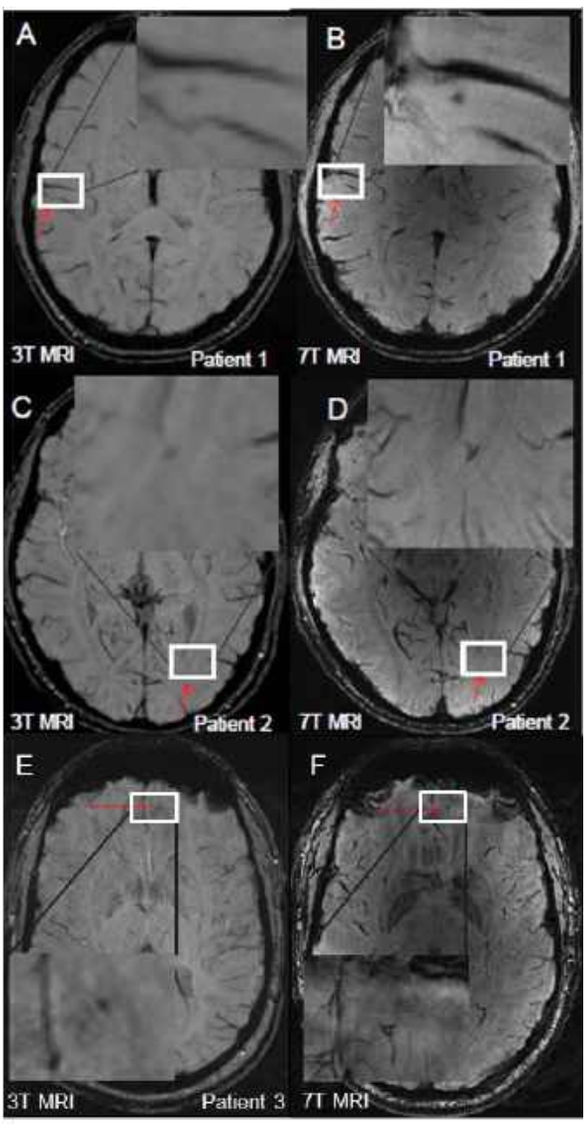

Figure 2: Comparison between pre-season 3T and 7T SWI for three AFP. Patient 1 shows a CM at 3T (A), which was confirmed at 7T (B). In addition two further adjacent CM were detected at 7T in this subject. Patient 2 showed a CM on the left occipital pole at 3T in (C), which was identified as an atypical small intracerebral vein at 7T (D). A third CM apparently detected within the left frontal lobe in patient 3 at 3T (E), also presented as a small atypical intracerebral vein at 7T (F).

intracerebral veins (Figues 1 D and F). As an additional finding a developmental venous anomaly (DVA) was found in one the AFP, which was well delineated in both 3T and 7T, whereas at 7T a more exact architecture of the DVA was definable. Post-season evaluations are still pending. Practically no differences between AFP and controls were found in the neuropsychological tests for the pre-season tests. Only in the Rey-Osterrieth Complex Figure Test in which subjects are asked to reproduce a complicated line drawing, first by copying it freehand (recognition), and then drawing from memory (recall), did the AFP perform significantly better than the controls. Group differences in verbal memory performance (verbal learning and memory test) and visual memory performance were not significant. In a brief test for the detection of memory and attention disorders, both groups showed similar noticeable results, which could indicate a slight cognitive impairment. There were significant group differences in the Beck Depression Inventory test, but no values that would speak for minimal depression were achieved.

7T SWI improves the depiction of CM. Moreover, 7T SWI allows a more accurate differentiation of lesions that were described as CM at 3T but were then identified as atypical venous blood vessels at 7T SWI. There have been isolated differences between the two groups in the evaluations of the neuropsychological tests performed in the baseline examinations so far, but no clear profile emerges. These are preliminary results from an ongoing study and results assessment. After further evaluating the post-season tests and imaging, as well as in comparison to the control group, a more detailed picture is expected.

References: 1. Hirad AA, et al. A common neural signature of brain injury in concussion and subconcussion. Sci Adv. 2019; 5(8):eaau3460. 2. Casson IR, et al. Is There Chronic Brain Damage in Retired NFL Players? Neuroradiology, Neuropsychology, and Neurology Examinations of 45 Retired Players. Sports Health. 2014; 6(5):384-95. 3. Moenninghoff C, et al. Diffuse axonal injury at ultra-high field MRI. PLoS One. 2015; 10(3):e0122329.

Neural Mechanisms for Accepting and Rejecting Artificial Social Partners in the Uncanny Valley

Would you trust a robot to make decisions for you? Autonomous artificial agents are increasingly entering our lives, but how the human brain responds to these new artificial social partners remains unclear. The uncanny valley (UV) hypothesis predicts that humans prefer anthropomorphic agents but reject them if they become too humanlike—the so-called UV reaction.

Using fMRI, we investigated neural activity when subjects evaluated artificial agents and made decisions about them. In the first task (cf. Figure 1), participants were shown a number of images that included humans, artificial humans, android robots, humanoid robots and mechanoid robots, and were asked to rate them in terms of likeability and human-likeness. Then, in a second task (cf. Figure 2), the participants were asked to decide which of these agents they would trust to select a personal gift for them, a gift that a human would like. Here, we found that participants generally preferred gifts from humans or from the more human-like artificial agents – except those that were closest to the human/non-human boundary, in-keeping with the Uncanny Valley phenomenon.

Across the two experimental tasks, the ventromedial prefrontal cortex (VMPFC) encoded an explicit representation of subjects' UV reactions. Specifically, VMPFC signaled the subjective likability of artificial agents as a nonlinear function of humanlikeness, with selective low likability for highly humanlike agents. In exploratory across-subject analyses, these effects explained individual differences in psychophysical evaluations and preference choices. Functionally connected areas encoded critical inputs for these signals: the temporoparietal junction encoded a linear humanlikeness continuum, whereas nonlinear representations of humanlikeness in dorsomedial prefrontal cortex (DMPFC) and fusiform gyrus emphasized a human–nonhuman distinction. Following principles of multisensory integration, multiplicative combination of these signals reconstructed VMPFC's valuation function. During decision making, separate signals in VMPFC and DMPFC encoded subjects' decision variable for choices

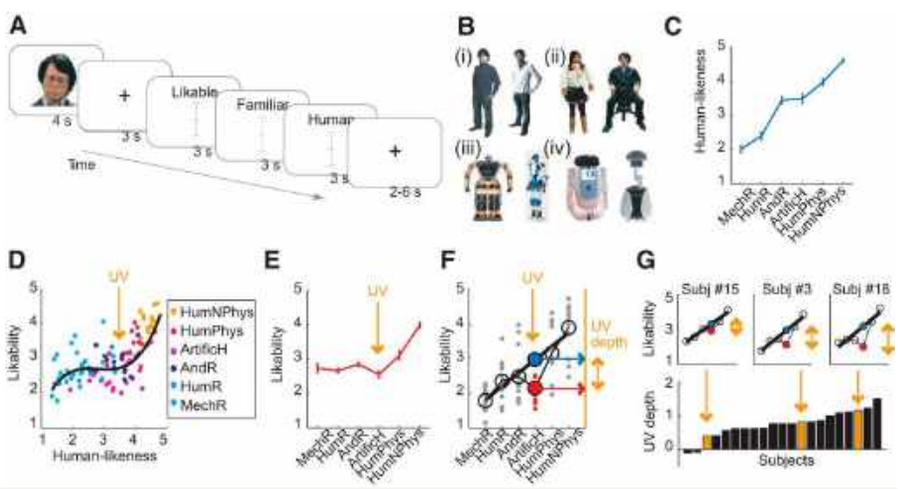

Behavioral UV reactions. A, Rating task. Subjects evaluated UV-relevant dimensions of humans and artificial agents. B, Example stimuli. (Bi) Artificial humans; (Bii) androids; (Biii) humanoid robots; (Biv) mechanoid robots. Human examples are not shown. C, Humanlikeness ratings for stimulus categories (MechR: mechanoid robots; HumR: humanoid robots; AndR: android robots; ArtificH: artificial humans; HumPhys: humans with physical impairments; HumNPhys: humans without physical impairments). Relatively lower ratings were found for HumNPhys compared with HumPhys due to lower familiarity (see text). D–G, UV effect in likability. D, Likability ratings for all stimuli. Black line: third-order polynomial fit (R2 = 0.573). E, Likability for artificial humans showed the UV-characteristic drop, indicating deviation from linear relationship between humanlikeness and likability. F, Quantifying UV depth. UV definition in single subject's likability ratings. Black line: linear regression-fit of likability to humanlikeness continuum from all stimuli (gray data) except UV-relevant artificial humans (red data). Blue point: predicted likability for artificial humans from linear fit; red point: observed likability. UV depth defined as difference between predicted and observed likability. G, UV depths across subjects. The procedure in F defined UV depths, illustrated for three individual subjects (top) and all subjects (bottom; p = 3.47 × 10−8, one-sample t test). UV effects were not found in several controls (e.g., humanoid robots; p > 0.15, one-sample t test). Error bars indicate SEM.

Astrid M. Rosenthal-von der Pütten, Nicole C. Krämer, Stefan Maderwald, Matthias Brand and Fabian Grabenhorst

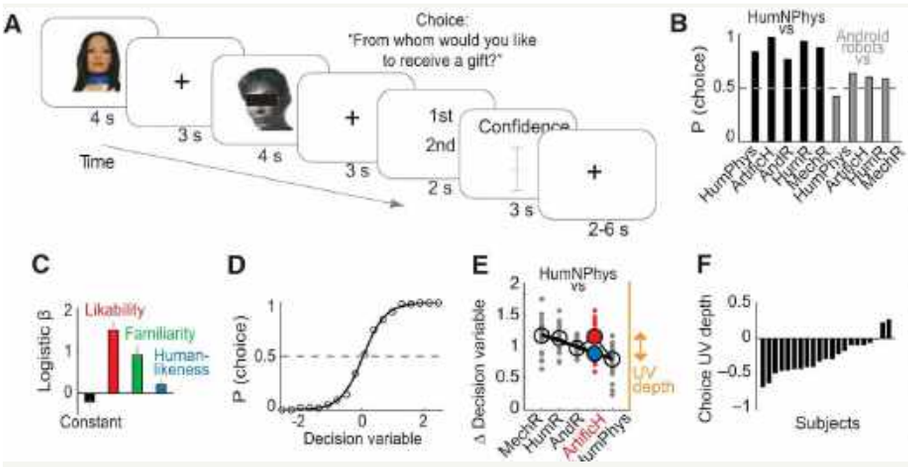

Decision making to accept or reject artificial agents. A, Choice task. Subjects viewed sequential stimuli and decided from whom they would like to receive a gift (example from categories android robots (first screen) and artificial humans (second screen); shown without black bar during the experiment. B, Choice behavior. Probability for gift-acceptance from humans (blacks) and androids (gray) over other stimulus categories. C, Modeling choices with logistic regression. β weights of relative likability, familiarity and humanlikeness (all $p < 0.002$, ones-sample t tests). D, Psychometric function: Relation between decision variable and choice probability. Relative differences in likability, familiarity and humanlikeness were weighted for individual subjects, based on subject-specific logistic regression, and summed to form a decision variable. Choice probabilities calculated for equally populated decision-variable bins and fitted with logit function. E, Defining UV depth for the choice task, based on decision variable. Unsigned (absolute) differences in decision variable between stimulus categories (Δ Decision Variable, derived from stimulus-specific ratings during rating task; data for all subjects). Black line: linear regression-fit to humanlikeness continuum for all conditions (gray data) except choices involving artificial humans (red data). Blue point: predicted decision variable for artificial humans from linear fit; red point: observed decision variable. Choice UV depth defined as difference between predicted and observed decision variable. F, Choice UV depth across subjects. The procedure in F defined UV depths for all subjects ($p = 1.1 \times 10-4$, one-sample t test).

involving humans or artificial agents, respectively. A distinct amygdala signal predicted rejection of artificial agents. Our data suggest that human reactions toward artificial agents are governed by a neural mechanism that generates a selective, nonlinear valuation in response to a specific feature combination (humanlikeness in nonhuman agents). Thus, a basic principle known from sensory coding—neural feature selectivity from linear–nonlinear transformation—may also underlie human responses to artificial social partners.

The results could have implications for the design of more likable artificial agents. We know that valuation signals in the identified brain regions can be changed through social experience. If you experience that an artificial agent makes the right choices for you - such as choosing the best gift - then your ventromedial prefrontal cortex might respond more favourably to this new social partner. Moreover, this is the first study to show individual differences in the strength of the Uncanny Valley effect, meaning that some individuals react overly and others less sensitively to human-like artificial agents. This means there is no one robot design that fits—or scares—all users. In my view, smart robot behaviour is of great importance, because users will abandon robots that do not prove to be smart and useful. This work has been published in the Journal of Neuroscience and was part of the dissertation of Astrid Rosenthal-von der Pütten at University of Duisburg-Essen. It received notable media attention with coverage in daily news such as dailymail.uk or focus.de and technology and science magazines such as inverse.com, neuroscience-news.com or earth.com.

References: 1. Rosenthal-von der Pütten, AM et al. Neural Mechanisms for Accepting and Rejecting Artificial Social Partners in the Uncanny Valley. Journal of Neuroscience; 1 July 2019; DOI: 10.1523/JNEUROSCI.2956-18.2019

Current Grants

Harald H. Quick: DFG: **Großgeräteantrag 7 Tesla MRT**

The aim of this project is to replace the 7 Tesla MRI system at the ELH.

T. W. Scheenen, J. J. Fütterer, F. Witjes, M. Sedelaar, M. Maas, J. O. Barentsz, D. W. J. Klomp, H. H. Quick: Radboudumc: **A personalized image-based assessment of metastatic potential of prostate cancer** (2018-2021)

In this grant the assessment of the aggressiveness of localized prostate cancer is correlated and validated with early detection of the first metastases of the disease.

N. Axmacher, D. Timmann, H. H. Quick: DFG-SFB 1280: F02 - **Focus group Neuroimaging: Extinction network connectivity across learning paradigms** (2017-2021)

In this joined project between PIs of the RUB and UKE, metaanalyses will be performed of fMRI data acquired in SFB1280. The main aim is to systematically investigate structural and functional extinction network connectivity across different learning paradigms and subject populations.

D. Timmann, H. H. Quick: DFG-SFB 1280: A05: **The contribution of the cerebellum to extinction: intrinsic mechanisms and cerebello-cerebral-interactions** (2017-2021)

The main aim of the project is to provide experimental evidence that the cerebellum has to be included as part of the neural circuitry underlying extinction of conditioned fear responses.

P. J. Koopmans: DFG Emmy Noether Programme – Independent Junior Research Group: **Functional Magnetic Resonance Imaging of cortical layers to measure directionality of information flow in brain networks for pain** (2017-2022)

Dr. Koopmans proposal focuses on the development of a high-resolution fMRI technique to improve understanding of how the brain processes pain.

T. W. Scheenen, H. H. Quick, J. O. Barentsz: Radboudumc: **Nanotechnology at ultra-high magnetic field: towards in vivo detection of small lymph node metastases with MRI** (2016–2020)

In this project the highest sensitivity of 7T to detect in vivo small lymph node metastases will be validated with histopathology of resected tissues in patients with rectal cancer.

M. E. Ladd, H.H. Quick, O. Speck: DFG: **German ultra-high field imaging (GUFI)**, Core Facility (2016-2020)

Aim of this project is to maintain and expand a nationwide network of UHF-MRI sites.

Erwin L. Hahn Lecture 2019

Keynote speaker Prof. Dr. Heidi Johansen-Berg from the University of Oxford, delivering an exciting lecture on studying connectivity and plasticity in the human brain with MRI.

Dr. Stefan G. H. Rietsch receives the ELH Young Scientist Award from his mentor Prof. Dr. Harald H. Quick for his thesis “Development and Evaluation of Radio Frequency Antennas for 7 Tesla Ultrahigh-Field Magnetic Resonance Imaging”.

Personnel and Organisational Structure at ELH

Directorate / Principal Investigators

Managing Director/PI
Prof. Dr. Matthias Brand

Directors/PIs
Prof. Dr. David G. Norris
Prof. Dr. Harald H. Quick

PIs
Prof. Dr. Ulrike Bingel
Prof. Dr. Dr. h.c. Onur Güntürkün
Dr. Tom W. J. Scheenen

Associated PIs
Dr. Peter J. Koopmans
Prof. Dr. Mark E. Ladd

Management

Administrative Director
Judith Kösters

Staff Scientist
Dr. Oliver Kraff
Dr. Stefan Maderwald

Assistance
Sigrid Radermacher

Public Relations
Stefanie Zurek

Scientists

Dr. Stephanie Antons
Giorgi Batsikadze, PhD
MSc. Jacob Bellmund
Dr. Andreas Deistung
Dr. med. Cornelius Deuschl
Dipl.-Phys. Thomas Ernst
Dr. rer. nat. Marcel Gratz
Dr Med. Tijmen Koëter
Dr. Irati Markuerkiaga
Dr. Bernhard Müller
Dr. Silke M. Müller
Dr. Stephan Orzada
MSc. Viktor Pfaffenrot
Dr. Stefan H. G. Rietsch
Dr. René Scheeringa
Dr. Jennifer Schulz
MSc. Daniel Sharoh
MSc. Tobias Spronk
Dr. Emma Sprooten
Dr. Katrin Starcke
Dr. med. Rutger Stijns
MSc Carlijn Tenbergen
Prof. Dr. med. Indira Tendolkar
Dr. Jan-Willem Thielen
Dr. Patrick Trotzke
Dipl.-Ing. Maximilian Völker

Students

Mahmoud Bagheri
Michael Klein
Larissa Meding

New in 2019

Mahmoud Bagheri
Michael Klein
Tijmen Koëter
Bernhard Müller
René Scheeringa

Left in 2019

Irati Markuerkiaga
Larissa Meding
Sigrid Radermacher
Stefan Rietsch
Rutger Stijns

Participation at ISMRM 2019 in Montréal, Canada

Dr. Marcel Gratz: "Performance analysis and optimization of MR-based attenuation correction in hybrid PET/MR" (ePoster)

Prof. Dr. Harald H. Quick: "High Field Imaging"

Dr. Oliver Kraff: "Clinical shoulder MR imaging at 7 Tesla in comparison to arthroscopy and 1.5 Tesla MRI"

Prof. Dr. Mark E. Ladd: "Expanding Access to UHF-MR: Major Concerns & Developing Guidelines"

Dr. Stefan Rietsch: "A 32-channel transmit/receive radiofrequency head coil for 7T UHF MRI"

Dr. Stefan H.G. Rietsch: "Quality assurance of 8-channel transmit/receive switches for a 32-channel transmit/receive system at 7T UHF MRI"

Seyedmorteza Rohani Rankouhi: "Detecting contaminants with long T2 relaxation time at 3 ppm in the human brain using the novel antiphase J difference editing method implemented in proton MRS at 7T"

Seyedmorteza Rohani Rankouhi: "Macromolecule free measurement of GABA with MASE-sLASER and ME-GA-sLASER sequences in the human brain at 7T"

Prof. Dr. Tom W.J. Scheenen: In vivo MR imaging of pelvic lymph nodes at ultra-high magnetic field (7T)

Daniel Sharoh: "Whole brain depth-dependent task based connectivity with laminar fMRI"

Maximilian N. Völker: "The traveling heads 2.0: Reproducibility of quantitative imaging methods at 7 Tesla"

Invited Talks and Workshops 2019

Dr. Oliver Kraff: "Exploring Implant Safety & Its Management: Ensuring Access"
ISMRM Workshop on Ultrahigh Field Magnetic Resonance, Cavtat, Croatia, 31 March - 03 April 2019

Dr. Oliver Kraff: "MR Safety Physics for 7T MRI"
ISMRM Workshop on MR Safety, Utrecht, The Netherlands, 20-22 September 2019

Dr. Stephan Orzada: "Pushing the Limits with pTx: System Considerations & Exam Supervision"
ISMRM Workshop on Ultrahigh Field Magnetic Resonance, Cavtat, Croatia, 31 March - 03 April 2019

Publications on 7T MRI

Ernst, T. M.; Brol, A.E.; Gratz, M.; Ritter, C.; Bingel, U.; Schlamann, M.; Maderwald, S.; Quick, H.H.; Merz, C.J.; Timmann, D. The cerebellum is involved in processing of predictions and prediction errors in a fear conditioning paradigm. (2019) *eLife* 8

Hong, D.; Asten, J.J.Av.; Rankouhi, S.R.; Thielen, J.; Norris, D.G. Effect of linewidth on estimation of metabolic concentration when using water lineshape spectral model fitting for single voxel proton spectroscopy at 7 T. (2019) *Journal of Magnetic Resonance* 304

Hong, D.; Rankouhi, S.R.; Thielen, J.; Asten, J.J.Av.; Norris, D.G. A comparison of sLASER and MEGA-sLASER using simultaneous interleaved acquisition for measuring GABA in the human brain at 7T. (2019) *PloS one* 14(10)

Kraff, O.; Quick, H.H. Radiofrequency Coils for 7 Tesla MRI. (2019) *Topics in Magnetic Resonance Imaging* 28(3)

Kraff, O.; Quick, H.H. [Safety of implants in high field and ultrahigh field MRI]. (2019) *Der Radiologe*

Meyer, M.C.; Scheeringa, R.; Webb, A.G.; Petridou, N.; Kraff, O.; Norris, D.G. Adapted cabling of an EEG cap improves simultaneous measurement of EEG and fMRI at 7T. (2019) *Journal of Neuroscience Methods* 331

Noureddine, Y.; Kraff, O.; Ladd, M.E.; Wrede, K.; Chen, B.; Quick, H.H.; Schaefers, G.; Bitz, A.K. Radiofrequency induced heating around aneurysm clips using a generic birdcage head coil at 7 Tesla under consideration of the minimum distance to decouple multiple aneurysm clips. (2019) *Magnetic Resonance in Medicine* 82(5)

Orzada, S.; Solbach, K.; Gratz, M.; Brunheim, S.; Fiedler, T.M.; Johst, S.; Bitz, A.K.; Shooshtary, S.; Abuelhaija, A.; Völker, M.N.; Rietsch, S.H.G.; Kraff, O.; Maderwald, S.; Flöser, M.; Oehmigen, M.; Quick, H.H.; Ladd M.E. A 32-channel parallel transmit system add-on for 7T MRI. (2019) *PLoS One* 14(9)

Philips, B.W.J.; Uden, M.Jv.; Rietsch, S.H.G.; Orzada, S.; Scheenen, T.W.J. A multitransmit external body array combined with a 1 H and 31 P endorectal coil to enable a multiparametric and multimetabolic MRI examination of the prostate at 7T. (2019) *Medical Physics*

Philips, B.W.J.; Stijns, R.C.H.; Rietsch, S.H.G. ;Brunheim, S.; Barentsz, J.O.; Fortuin, A.S.; Quick, H.H.; Orzada, S.; Maas, M.C.; Scheenen, T.W.J. USPIO-enhanced MRI of pelvic lymph nodes at 7-T: preliminary experience. (2019) *European Radiology*

Rietsch, S.H.G.; Brunheim, S.; Orzada, S.; Völker, M.N.; Maderwald, S.; Bitz, A.K.; Gratz, M.; Ladd, M.E.; Quick, H.H. Development and evaluation of a 16-channel receive-only RF coil to improve 7T ultra-high field body MRI with focus on the spine. (2019) *Magnetic Resonance in Medicine*

Rosenthal-von der Pütten, A.M.; Krämer, N.C.; Maderwald, S.; Brand , M.; Grabenhorst, F. Neural Mechanisms for Accepting and Rejecting Artificial Social Partners in the Uncanny Valley (2019) *Journal of Neuroscience* 39 (33)

Sato, T.; Matsushige, T.; Chen, B.; Gembruch, O.; Dammann, P.; Jabbarli, R.; Forsting, M.; Junker, A.; Maderwald, S.; Quick, H.H.; Ladd, M.E.; Sure, U.; Wrede, K.H. Wall Contrast Enhancement of Thrombosed Intracranial Aneurysms at 7T MRI. (2019) *American Journal of Neuroradiology* 40(7)

Sinnecker, T.; Hadisurya, J.; Schneider-Hohendorf, T.; Schwab, N.; Wrede, K.; Gembruch, O.; Gold, R.; Hellwig, K.; Pilgram-Pastor, S.; Adams, O.; Albrecht, P.; Hartung, H.; Aktas, O.; Kraemer, M. Extensive immune reconstitution inflammatory syndrome in Fingolimod-associated PML: a case report with 7 Tesla MRI data. (2019) *BMC Neurology* 19(1)

Thielen, J.; Gancheva, S.; Hong, D.; Rankouhi, S.R.; Chen, B.; Apostolopoulou, M.; Anadol-Schmitz, E.; Roden, M.; Norris, D.G.; Tendolkar, I. Higher GABA concentration in the medial prefrontal cortex of Type 2 diabetes patients is associated with episodic memory dysfunction. (2019) *Human Brain Mapping*

Awards

Dr. Oliver Kraff: ISMRM Distinguished Reviewer Award

Dr. Oliver Kraff: DAAD Travel Grant for participation at the 2019 annual ISMRM symposium

Dr. Stephan Orzada: ISMRM Distinguished Reviewer Award

Dr. Stefan H. G. Rietsch: ELH-Award 2019 for Dissertation Thesis: "Development and Evaluation of Radio Frequency Antennas for 7 Tesla Ultrahigh-Field Magnetic Resonance Imaging"

Prof. Dr. Harald H. Quick: "Best Teacher Award", Fachschaft Bachelor Degree Programme, Medizintechnik, University of Duisburg-Essen

Prof. Dr. Harald H. Quick and Dr. Oliver Kraff received an award from the Wiley Online Library, as between 2017 and 2018 their publication "7T: Physics, safety, and potential clinical applications" (originally published in the Journal for Magnetic Resonance Imaging) was among the top downloaded papers.

Prof. Dr. Mark Ladd: President of the German Society for Medical Physics (Deutsche Gesellschaft für Medizinische Physik, DGMP)

Prof. Dr. Mark Ladd: Nomination for the German President's Award for Innovation in Science and Technology (Deutscher Zukunftspreis)

Prof. Dr. Mark Ladd: Member of the Annual Meeting Program Committee of ISMRM

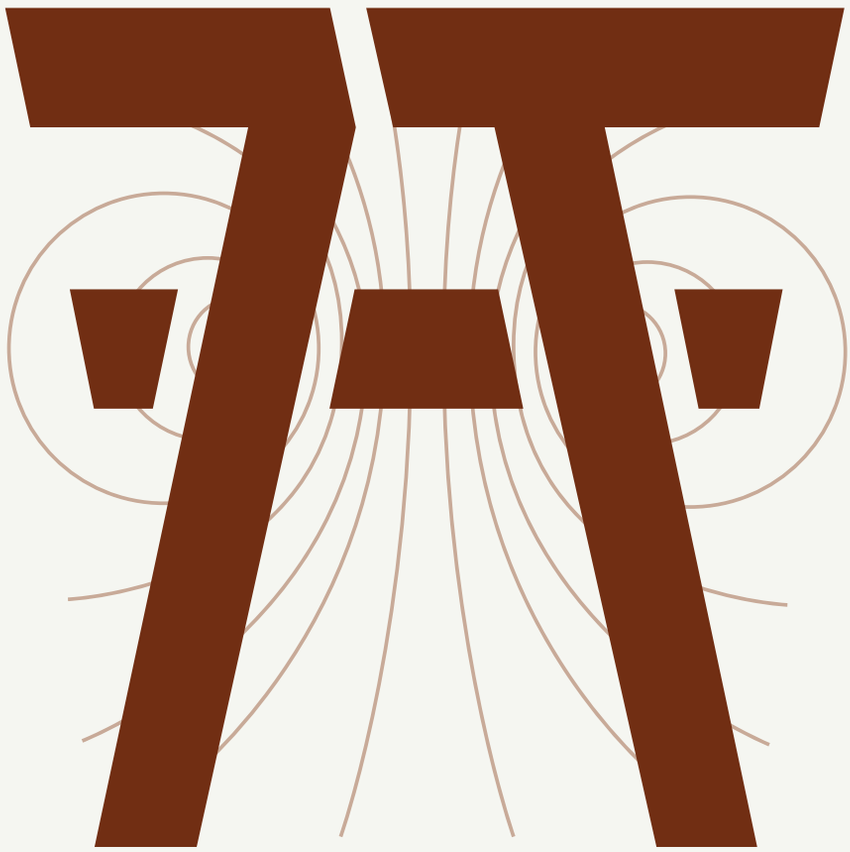

Universität Duisburg Essen
Open-Minded

Ruhr Universität Bochum
RUB

UMC St Radboud

Universität Duisburg Essen
Ingenieurwissenschaften

Donders Institute
for Brain, Cognition and Behaviour

Universitätsklinikum Essen

Radboud Universiteit